Biaxial strain engineering of charge ordering and orbital ordering in $HoNiO_3$

Li-tong Jiang,[1,2] Kui-juan Jin,[1,2,3,*] Chao Ma,[1] Chen Ge,[1] Guo-zhen Yang,[1,2,3] and Xu He[1,4]

[1]*Beijing National Laboratory for Condensed Matter Physics, Institute of Physics, Chinese Academy of Sciences, Beijing 100190, China*

[2]*University of Chinese Academy of Sciences, Beijing 100049, China*

[3]*Collaborative Innovation Center of Quantum Matter, Beijing 100190, China*

[4]*Theoretical Materials Physics, Q-MAT, CESAM, University of Liège, B-4000 Liège, Belgium*

(Received 8 January 2018; revised manuscript received 8 April 2018; published 16 May 2018)

Strain in epitaxial $HoNiO_3$ is found to be capable of influencing the charge and the spin of Ni ions and the orbital hybridization of Ni-O and further manipulating charge ordering and orbital ordering by our first-principles calculation. The tensile strain can encourage Jahn-Teller distortion instead of breathing distortion, which leads to the phase transition from the charge-ordering state to the orbital-ordering state. Furthermore, we calculated the potential energy of the two modes, which reveals that the biaxial strain tunes the competition between the breathing and Jahn-Teller distortions.

DOI: 10.1103/PhysRevB.97.195132

I. INTRODUCTION

$HoNiO_3$ (HNO) is one of the perovskite rare-earth nickelates in the chemical formula family of $RNiO_3$ (RNO), where R = La, Pr, Nd, Sm, Eu, ..., Lu. In this material family, the interplay of lattice structure and electronic configurations controls the charge, orbital, and spin [1]. HNO undergoes a first-order metal-insulator phase transition (MIT) at a temperature $T_{MI} \sim 570$ K by lowering the symmetry from an orbital-ordering (OO) orthorhombic $Pbnm$ phase to the ground state of a charge-ordering (CO) monoclinic $P2_1/n$ phase [2–4]. The CO state in $P2_1/n$ is accompanied by a breathing distortion which breaks up the equivalent Ni sites into two nonequivalent sites by a Ni-O bond length disproportionation with alternating octahedra of Ni ions with shorter bonds (Ni_S) and those with longer bonds (Ni_L).

The electronic structure in the $P2_1/n$ phase has been controversial. Usually, the oxidation states of Ni in HNO are +3, corresponding to the $3d^7$ electronic configurations of Ni ions [1]. It was sometimes interpreted as $2\times(d^7) \rightarrow d^8 + d^6$ at Ni sites [5]. Nowadays, the configuration of $P2_1/n$ is more often viewed as $2\times(d^8\underline{L}) \rightarrow d^8 + d^8\underline{L}^2$ [6,7], with $\underline{L}$ denoting a ligand hole on the oxygen site [8]. In the $Pbnm$ phase, the Ni ion is usually taken to be $3d^7$ or $3d^8\underline{L}$. Some results stress the exquisite sensitivity of the electronic structure to various types of structural distortion, including Jahn-Teller (JT) distortion and breathing-mode distortion, under the epitaxial constraint [9–12].

As the epitaxial growth on a single-crystalline substrate forces the film to have the same in-plane lattice parameters as those of the substrate, including distortions, lattice symmetry, octahedral tilts, and rotations, thin films grown on a substrate become different from their bulk counterpart [13]. The distorted [NiO_6] octahedra with different in-plane and out-of-plane Ni-O bonds can result in finite orbital polarization under a biaxial strain [1]. The JT [14] and breathing-mode distortions [15] are coupled to the octahedral rotation. As the tensile biaxial strain can modulate the rotation modes and Ni-O-Ni bond angles, it may tune the competition between the breathing-mode and JT-mode distortions [16].

In this paper, we report that the strain can manipulate the transition between CO ($P2_1/n$) and OO ($Pbnm$) for HNO, accompanied by the charge transfer during the corresponding phase-transition process based on the results calculated from density functional theory (DFT). We will also show how and why the strain modifies the orbital hybridization and the electronic configurations and further affects the spin and orbital by changing the in-plane biaxial strain in HNO. This work should shed a light on how to manipulate CO ($P2_1/n$) and OO ($Pbnm$) in HNO thin films epitaxially grown on different substrates with various biaxial strains.

II. METHOD

The first-principles calculations were performed with general-gradient-approximation-Perdew-Burke-Ernzerhof (PBEsol) and projector augmented-wave (PAW) method [17] as implemented in the Vienna Ab initio simulation package [18] (VASP). The energy cutoff is 500 eV. Here $3\times6\times2$ and $6\times6\times4$ Γ-centered k-point grids were used to integrate the Brillouin zone for the S-type antiferromagnetic (S-AFM) 80-atom structure and the A-type AFM (A-AFM) 20-atom structure, respectively. The S-AFM and A-AFM structures have wave vectors of (1/4, 1/4, 1/4) and (0, 0, 1/2), respectively. S-AFM magnetic order in $Pbnm$ and $P2_1/n$ forms in $+1+1-1-1$ and $+20-20$, respectively. S-AFM is the ground state in HNO. The PAW potentials of Ni ($3p3d$), Ho ($5p5d6s$), and O ($2s2p$) were used. A Hubbard-like correction [19] with U (Ni) = 2 eV was used to better describe the on-site electron-electron interaction in the transition-metal elements. Previous works showed that a small U can accurately describe the phase in nickelates [15,20,21]. Maximally localized Wannier functions were constructed

*Corresponding author: kjjin@iphy.ac.cn

using the WANNIER90 package [22]. The structures were relaxed totally to the criterion of the residual forces below 10^{-3} eV/Å. For the calculation of the structure with biaxial strain, the lattice constants a and b were fixed, while all the other degrees of freedom were fully relaxed. The symmetry-adapted mode analysis implemented in ISODISTORT [23] was used to calculate the amplitude of the lattice distortions. The reference high-symmetry structure was the $Pm\bar{3}m$ cubic phase.

We found the CO/OO phase transition happens in both S-AFM and A-AFM structures. For the calculation of energy wells versus lattice distortion and the dependence of the CO/OO phase transition on Hubbard U, an A-AFM was used as the representative structure. In $HoNiO_3$, the oxygen octahedra have an $a^-b^-c^+$ rotation pattern; therefore, films along the ab plane and the ac plane are not equivalent. Usually, thin films tend to be along the ab plane with tensile strain and along the ac plane with compressive strain, like $CaTiO_3$ and $SrRuO_3$ [24,25]. For an ab-orientated structure, we use a $\sqrt{2}\times\sqrt{2}\times2$ supercell for the FM and A-AFM states; for the S-AFM state, we use a $2\sqrt{2}\times\sqrt{2}\times4$ supercell. For ac-orientated structures in FM and A-AFM states, a $2\times2\times2$ supercell is used; in the S-AFM state, a $2\sqrt{2}\times2\sqrt{2}\times4$ supercell is needed. Since the films along the ac plane are often less energetically favorable with tensile strain, we checked only the energies of the along-ac plane with various magnetic orders at $\epsilon = 5\%$. We calculated the structure of HNO; the lattice parameters of the $P2_1/n$ ($\sqrt{2}\times\sqrt{2}\times2$) structure are $a = 5.46$ Å, $b = 5.09$ Å, $c = 7.31$ Å, $\alpha = \gamma = 90^\circ$, and $\beta = 89.99^\circ$, which are very close to the experimental results ($a = 5.51$ Å, $b = 5.18$ Å, $c = 7.42$ Å) [26]. We take the in-plane pseudocubic lattice parameter $a' = 3.72$ Å as half of the diagonal of a and b ($a' = \sqrt{a^2 + b^2}/2$), which is the reference value for the strain. The biaxial tensile strain on a substrate with in-plane parameter a_{sub} is characterized by lattice mismatch $\epsilon = (a_{sub} - a')/a'$, where a' and a_{sub} are the pseudocubic lattice constants of HNO and the substrate, respectively.

III. RESULTS

We plot the results of the energy and band gap of HNO under in-plane biaxial strain in Figs. 1(a) and 1(b). We can see that there is a first-order phase transition between $P2_1/n$ and $Pbnm$ by the energy of HNO under biaxial strain in the ab plane $\epsilon = 4.8\%$, which is about $a_{sub} = 3.90$ Å. It should be noted that the S-AFM magnetic order lowers the $Pbnm$ symmetry to $P2_1/n$. However, we found that the distortions of the structures relaxed from a $Pbnm$ structure are more similar to the $Pbnm$ bulk structure than the $P2_1/n$ structure; that is, there is a JT distortion, whereas the breathing-mode distortion is vanishingly small. Therefore, we still use the notation $Pbnm$ to denote this state, while we use $P2_1/n$ to denote the state with charge disproportionation. The energy is lower in the $P2_1/n$ phase below that tensile strain, which means the CO $P2_1/n$ phase is favorable, while the OO $Pbnm$ phase is energetically favorable with ϵ larger than 4.8%.

We also calculated the ferromagnetic (FM) and A-AFM structures and found that the CO/OO phase transition persists. We also checked the structures along the ac plane and found that their energies are indeed higher than those along the ab plane with tensile strain near the phase-transition point; that is, the ground state with enough tensile strain is the OO state along the ab plane. Therefore, we do not further discuss the structures along the ac plane and drop the ab and ac notation hereafter. The energies of the phases with various magnetic orders and film orientations at a tensile strain of 5% are shown in Table I. In addition, the $R\bar{3}c$ structure ($C2/c$ when the in-plane lattice parameters are fixed), which is the ground state of $LaNiO_3$, was also tested, and the energies were much higher than those of both CO and OO structures. The phase transition is accompanied by a change in the band gap, which decreases in the CO structure and increases in the OO structure gradually with the increasing of tensile strain, as shown in Fig. 1(b).

TABLE I. Energy of various phases at a tensile strain of 5%. The reference state (zero energy) is the S-AFM CO structure along the ab plane.

Phase	Plane	Magnetic order	Energy (eV)
$R\bar{3}c$		G-AFM	1.33
		FM	1.24
OO	ab	A-AFM	0.06
	ab	FM	0.05
	ab	S-AFM	0.00
	ac	A-AFM	0.35
	ac	FM	0.33
	ac	S-AFM	0.31
CO	ab	A-AFM	0.12
	ab	FM	0.11
	ab	S-AFM	0.01
	ac	A-AFM	0.37
	ac	FM	0.34
	ac	S-AFM	0.30

The phase transition persists within a large range of U (Ni) from 0 to 6 eV in Fig. 1(c). For the same strain, the larger U encourages the structure to perform OO and increases the energy difference between CO and OO, as shown in Fig. 1(c). This is consistent with the fact that the on-site Coulomb interaction could suppress the spatial charge fluctuation. Therefore, the Coulomb interaction favors a non-charge-ordered state [5].

We now explore the change in lattice distortion through the phase transition with the tensile strain. In HNO, the lattice deviates from the ideal cubic perovskite structure mainly by the following lattice distortions, namely, the $a^-a^-c^+$ oxygen octahedral rotations, the in-plane staggered JT distortions (labeled M_3^+ [23], in the OO phase), and the breathing-mode distortion (labeled R_2^-, in the CO phase). Here we use an A-site-oriented configuration for labeling the distortion modes in perovskites. For a B-site-oriented configuration, the corresponding labels of the JT and breathing modes are M_2^+ and R_1^+, respectively, which were used in Ref. [27]. There are multiple JT and breathing modes in perovskites; however, hereafter, we refer to the JT and breathing modes as the JT and breathing modes, respectively, because other types of JT and breathing modes are negligibly small in HNO. The JT mode can be characterized by the difference of in-plane Ni-O bond lengths in one Ni-O octahedron, whereas the breathing mode can be characterized

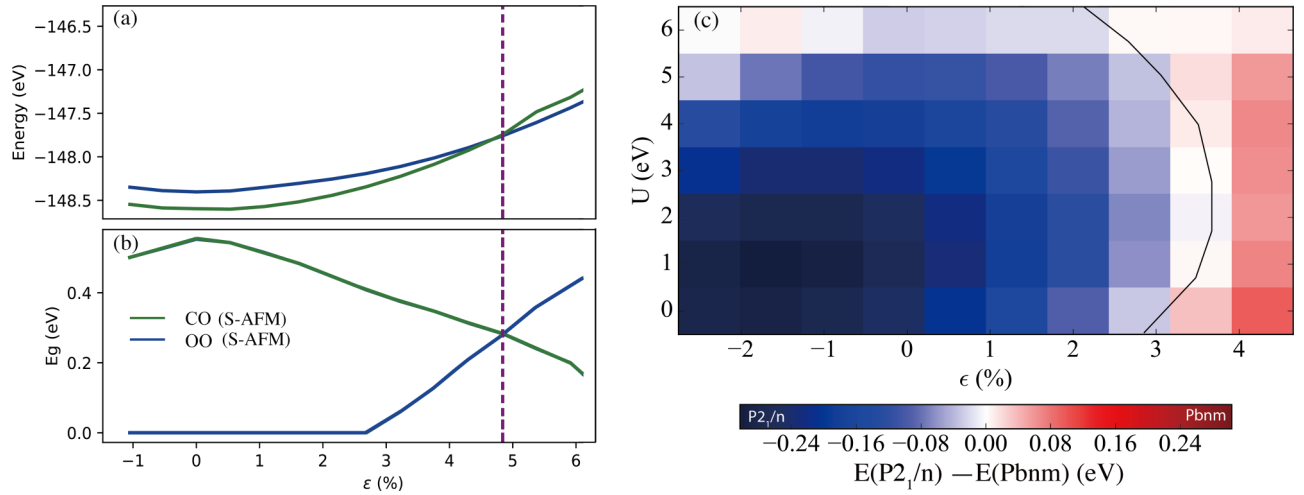

FIG. 1. (a) Energy versus tensile strain and (b) band gap versus tensile strain in the $Pbnm$ OO (S-AFM) phase (blue) and monoclinic $P2_1/n$ (S-AFM) phase (green). The energies are per 20-atom structure. (c) Lattice-mismatch-U phase diagram. The color bar shows the energy difference between $P2_1/n$ and $Pbnm$. (c) is calculated with an A-AFM structure. The black line denotes the phase-transition points.

by the difference of average Ni-O bond lengths between two neighboring Ni-O octahedra. Figure 2 demonstrates how the lattice mismatch impacts the lengths of bonds in Ni octahedra. We define the lengths of bonds in Ni-O in the x, y, and z directions as l_x, l_y, and l_z, respectively, as shown in Fig. 2(a). In the OO state, we use Ni_x for l_x being longer than l_y and Ni_y for l_y being longer than l_x. In Fig. 2(b), the increase in average bonds of l_x, l_y, and l_z means the octahedra expand with the increase in the tensile strain. There is no significant change in the difference between the average bond lengths for Ni_L and Ni_S in the CO phase. The breathing mode in CO abruptly decreases to zero in the OO phase. Meanwhile, the JT distortion is negligibly small in the CO phase, and it abruptly increases at the phase-transition point. In the $Pbnm$ phase, $|\,l_x\text{-}l_y\,|$ increases with the increment of tensile strain, as shown in Fig. 2(c). The Ni-O bonds in the z direction shrink with the tensile strain, as shown in Fig. 2(d).

For most epitaxial films, the in-plane biaxial strain affects the rotations of Ni octahedra. In Fig. 3(a), the Ni-O-Ni angles along l_x, l_y, and l_z are denoted θ_x, θ_y, and θ_z, respectively. It can be seen that θ_z is indeed affected by the strain, while the change in the in-plane Ni-O-Ni bond angles is relatively small in HNO. The charge and magnetic moment are depicted in Figs. 3(b) and 3(c), respectively. In all these structures, the $3d$ charges inside the Ni ion PAW spheres are about 8, while the Ni_S ions have a small magnetic moment. The results from Figs. 2(b) and 3(b) are consistent with the picture that the CO in nickelates is bond centered rather than charge centered, as is the case in OO.

To see how the breathing-mode and JT-mode distortions are coupled to the biaxial strain, we calculated the potential energy of the structures by varying the lattice distortions, as shown in Fig. 4. Since the rotations of the oxygen octahedra increase with the strain and are known to be strongly coupled with the breathing mode, we first try to see how the breathing and JT distortions are affected by the rotations. In Fig. 4(a), large distortion causes two single wells with electronic instability. The potential well is a single well with a rotation mode

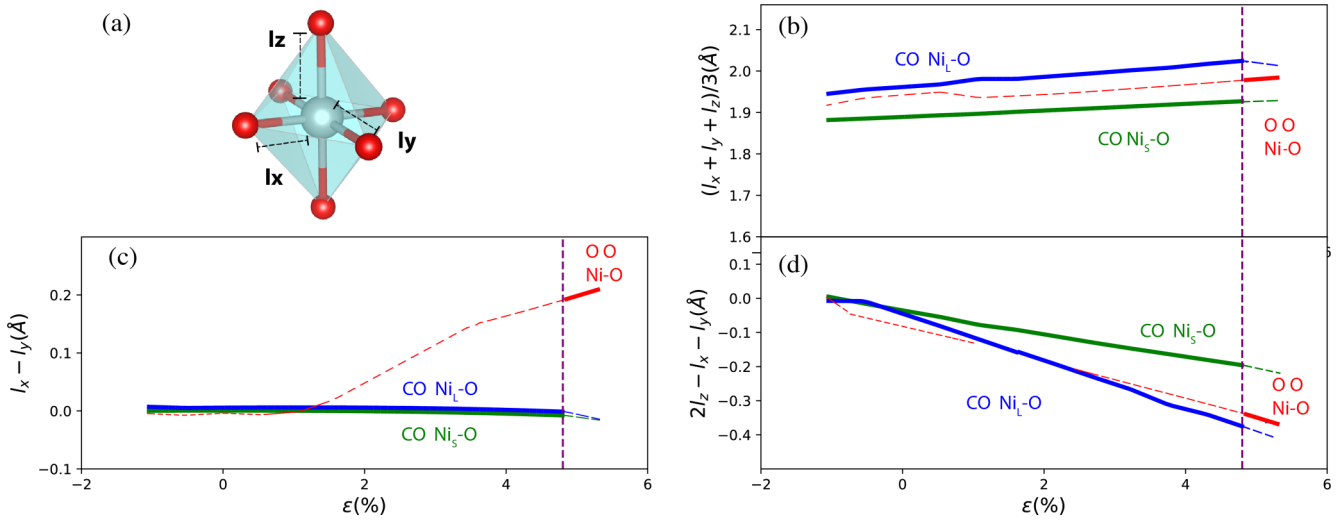

FIG. 2. Ni-O bond lengths as functions of tensile strain. (a) The bond lengths along each axis of an octahedron: l_x, l_y, and l_z. The average Ni-O bonds of (b) octahedra, (c) l_x-l_y, and (d) $2l_z$-l_x-l_y versus lattice mismatch.

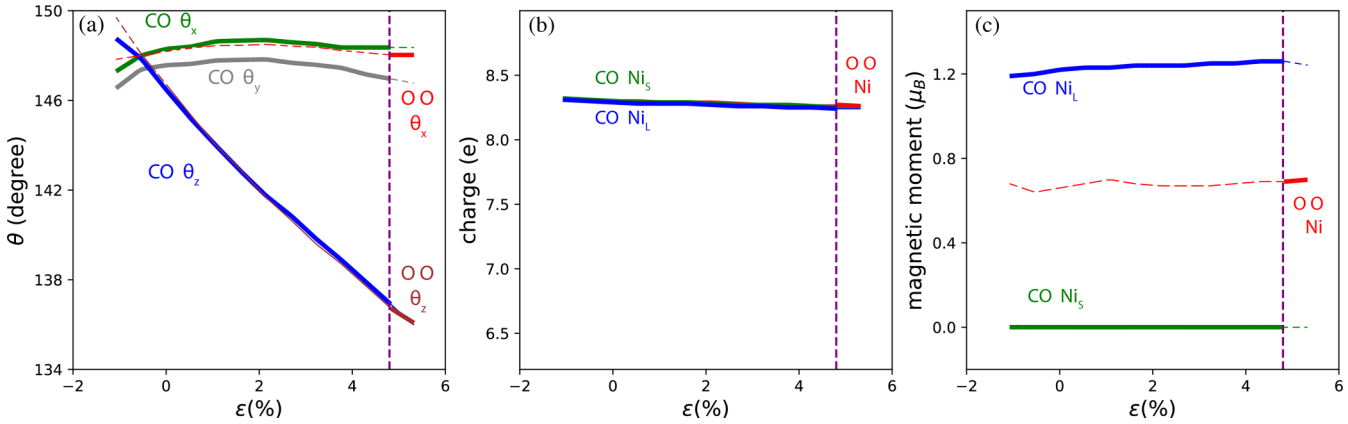

FIG. 3. (a) Bond angles of Ni-O-Ni, (b) charges in Ni ions, and (c) magnetic moment of Ni versus lattice mismatch.

below 66%. The single well becomes shallower as the rotation increases, showing the softening of the breathing mode, which also occurs in other nickelates [15]. It becomes two shifted single wells with a rotation mode larger than 66%, meaning the lowering of symmetry via the breathing-mode distortion, implying that there is an electronic instability which can be enhanced by the rotation modes. Figure 4(b) shows that JT mode is softened with rotation, which is also observed in other $Pbnm$ structures, like manganites [14]. It is also worth noticing that the potential well is asymmetric in Fig. 4(b) due to a trilinear coupling between the rotation modes and the JT mode, whose energy is proportional to $\Phi_{xy}^{-}\Phi_{z}^{+}Q_{2}^{+}$, where Φ_{xy}^{-}, Φ_{z}^{+}, and Q_{2}^{+} are the amplitudes of the antiphase rotations ($a^{-}a^{-}$), the in-phase rotation (c^{+}), and the JT modes, respectively [16,28]. (This term can also be interpreted as a quad-linear term since the Φ_{xy}^{-} mode can also be written as two antiphase rotations along Φ_{x}^{-} and Φ_{y}^{-}, e.g., as in Ref. [16].) This coupling breaks the $+Q_{2}^{+} \leftrightarrow -Q_{2}^{+}$ symmetry, making the double well asymmetric, as shown in Fig. 4. HNO favors the CO phase under the $a^{-}a^{-}c^{+}$ oxygen octahedral rotation, with no strain applied. It can be seen that the rotation enhances both the breathing mode and the JT mode.

Then we fix the rotations to 100% of the bulk value and calculate the energies with various tensile strains. In Fig. 4(c), with a larger tensile strain, the breathing-mode shifted single wells become shallower, meaning that the breathing mode is less favored. In Fig. 4(d), the JT mode is further softened and also becomes more asymmetrical with tensile strain, which eventually makes the JT mode favorable than the breathing mode. It can also be seen that the asymmetry of these two

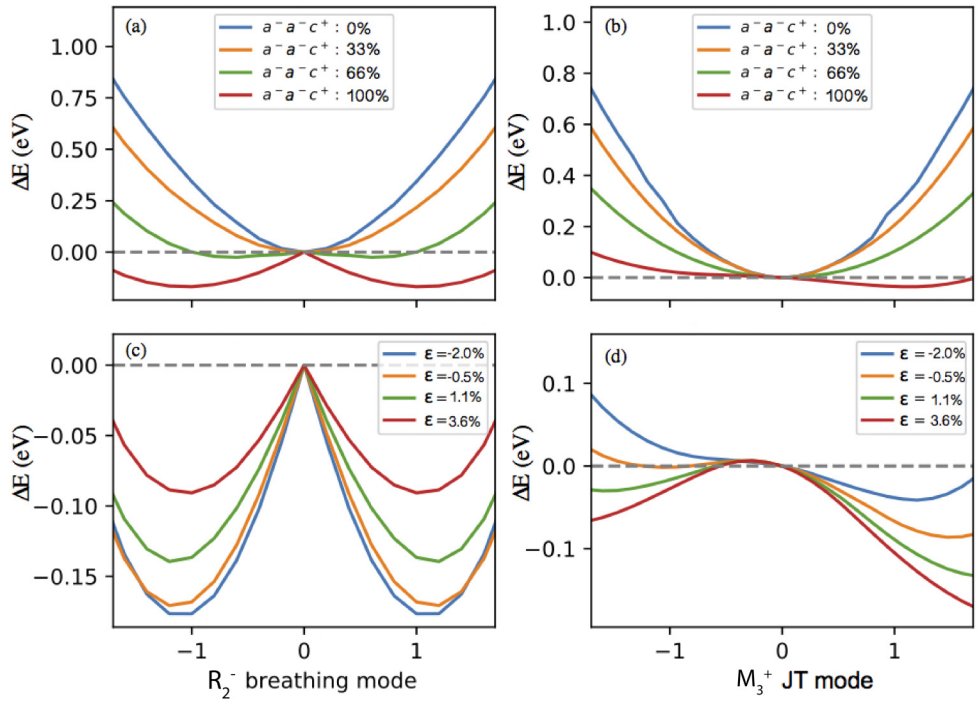

FIG. 4. Potential-energy wells (A-AFM) as functions of lattice distortions. (a) Energy versus the R_{2}^{-} breathing mode with various degrees of octahedral $a^{-}a^{-}c^{+}$ rotations. (b) Energy versus the M_{3}^{+} JT mode with various degrees of octahedral $a^{-}a^{-}c^{+}$ rotations. (c) Energy versus the R_{2}^{-} breathing mode with various biaxial strains. (d) Energy versus the M_{3}^{+} JT mode with various biaxial strains. Rotation to 100% means the bulk value.

single wells increases with the strain, indicating that although the rotation of $a^-a^-c^+$ alone cannot make the phase transition from the CO to OO phase, it does play a role in this phase-transition process.

The structural phase transition changes the electronic configuration, resulting in different spin, orbital, and charge properties. Figure 5 shows the electronic configurations of the CO and OO phases in HNO. Figures 5(a) and 5(b) schematically show the structure of Ni octahedra in the CO and OO phases, respectively, followed by the schematic electronic occupation in orbitals for Ni_S and Ni_L in CO and Ni_x and Ni_y in OO, respectively, which will be discussed in detail later. For the Ni_x in OO, the tensile strain could strengthen JT distortion, resulting in a bigger splitting of e_g, which enhances OO, as shown in Fig. 5. But for CO, the tensile strain suppresses CO, without the OO state.

A maximally localized Wannier function (MLWF) [22] analysis was used to present the electronic configurations in Fig. 5. The MLWFs were constructed from the occupied states. The inner (frozen) window and the outer window for constructing the MLWFs were both -8 to 0 eV relative to Fermi energy; that is, all the O $2p$ and Ni $3d$ orbitals in the valence states are included. Two sets of initial projections were tried. Both include all O $2p$ orbitals and all Ni t_{2g} orbitals. In addition, the first set has one e_g orbital on each Ni, which are in the major-spin channel and along the longest axis of the corresponding Ni-O octahedron, which represents a d^7/d^7 configuration. The second set of initial projections has two e_g orbitals in the Ni_L major-spin channel, while no e_g orbital is on the minor-spin channel, which represents a d^8/d^6 configuration. We imposed these two sets of initial projections on both charge-ordering and orbital-ordering structures and found that the d^7/d^7 configuration could be well localized in the orbital-ordered structure, whereas the d^8/d^6 configuration can be maximally localized in the charge-ordered structure. To plot the Wannier functions for other Ni e_g orbitals, we also constructed the Wannier functions from the conduction band with the frozen window from 0 to 2 eV and the outer window from 0 to 5 eV. Six t_{2g}-like MLWFs were found at each Ni site, and six O $2p$-like MLWFs were also found at each O site. In the $P2_1/n$ phase, there is no occupied e_g-like MLWF on the Ni_S site, while the O $2p$-like orbital has a large portion on its neighboring Ni_S site [Fig. 5(c)], showing that there is strong mixing between Ni_S e_g and O $2p$ orbitals. For Ni_L sites, two fully occupied e_g MLWFs are found [Figs. 5(d) and 5(e)]. The result is consistent with the Wannier function analysis of Ref. [20] in the CO phase in RNO. It should be noted that the Wannier functions assigned to the ions here are linked to the oxidation states rather than the number of electrons around the ions. In transitional oxide, the charges around the ions tend not to change even when the oxidation state becomes different [29]. The $3d$ charge densities around Ni_S and Ni_L are both around 8 in Fig. 3(b); therefore, the two sites can be viewed as d^8, but with different electronic configurations. The Ni_S and Ni_L ions have electron configurations of $3d^4\uparrow\ 3d^4\downarrow \underline{L}^2$ (with two e_g electrons shared with O $2p$) and $3d^5\uparrow\ 3d^3\downarrow$ (with two e_g electrons), respectively. Here $\uparrow$ is assumed to be the major-spin channel.

This electronic configuration is related to the breathing-mode distortion. Under the octahedron crystal field, the Ni^{3+} ion in octahedron [NiO_6] has seven d electrons, which would have an octahedral splitting diagram with six electrons in the t_{2g} levels and one electron in the e_g levels. For the CO phase, because of the Coulomb repulsion between the Ni e_g and O^{2-}, the splitting energy of e_g/t_{2g} in Ni_S is larger than that of Ni_L. This leads to different e_g energies in the two Ni sites and a charge disproportionation, as shown in Fig. 5 for the CO phase. The top of the valence band and the bottom of the conduction band are the Ni_L and Ni_S e_g bands, respectively. Therefore, the band gap resulting from this e_g energy difference is directly linked to the amplitude of the breathing mode. The larger breathing mode shifts the Ni_L e_g downward and the Ni_S e_g upward, so that it can increase the gap of the CO state. This can explain our calculated change in band gap in the CO phase in Fig. 1(b). The hybridization of Ni-O $2p$ depends on the distance between Ni and O, which means electrons in O $2p$ favor hybridizing with the e_g level in Ni_S, which compensates the charge disproportionation. A larger Ni-O octahedron would further localize the Ni_L e_g states and lead to a larger magnetic moment, which is shown in Fig. 3(c). These results support the previous view that CO is more likely the oxygen site or bond-centered $3d^8\underline{L} + 3d^8\underline{L} \rightarrow 3d^8 + 3d^8\underline{L}^2$[6–8,21].

In the OO phase, one e_g MLWF is found on each Ni site, which is the $d_{3x^2-r^2}$-like MLWF for Ni_x and the $d_{3y^2-r^2}$-like WF for Ni_y, as shown in Fig. 5(f). We also constructed the MLWFs from the conduction bands. The calculated MLWFs are $d_{y^2-z^2}$-like for Ni_x and $d_{z^2-x^2}$ for Ni_y, as shown in Fig. 5(g). Both of them show significant O $2p$ tails, suggesting these states are strongly hybridized with O $2p$ states. Since about eight $3d$ electrons are also found on each Ni site, the electronic configuration can be written as $d^8\underline{L}$.

Similarly, the neighboring Ni ion in the same xy plane (Ni_x) has elongated l_x. Therefore, the occupied e_g states are $d_{3x^2-r^2}$ and $d_{3y^2-r^2}$ alternately along the x and y directions [Figs. 5(f) and 5(g)]. The shorter bond of Ni-O has more charge transfer from O $2p$ to Ni $3d$, which causes the actual charge value to be more than 7 in the OO state [Fig. 3(b)]. For the Ni_x in OO, the tensile strain could strengthen the JT distortion, resulting in a bigger splitting of e_g levels, which enhances the OO [Fig. 5(b)]. The band gap is the e_g splitting, increasing with tensile strain in the OO structure [Fig. 1(b)].

The electronic configuration for the CO phase shown in Fig. 5 is further demonstrated in the orbital-projected electronic band structure in Figs. 6(a)–6(d). In Fig. 6(a), the colors show the projection to the four Ni_S e_g states (two e_g orbitals for each spin). While the majority of these orbitals are in the conduction band, the hybridized states between Ni_S e_g and O $2p$ are occupied. In Fig. 6(c), yellow and green denote the two Ni_L e_g states in the major-spin channel, which are mostly occupied. There is a splitting between the e_g spin-up and -down states in Ni_L. The Ni_L e_g states in red and blue about 3 eV above the Fermi energy do not show much mixing with the O $2p$ states below the Fermi energy.

The electronic configuration for the OO phase shown in Fig. 5 can also be proved from Figs. 6(e) and 6(f), where we find one e_g orbital in red ($d_{3x^2-r^2}$ on Ni_x in its major-spin channel) almost fully occupied, while the other three e_g states are mostly above the Fermi energy, meaning that they hybridize with O $2p$ states and have significant occupations. For the in-plane JT distortion, for example, in the case of $l_x > l_y$ [Ni_x in

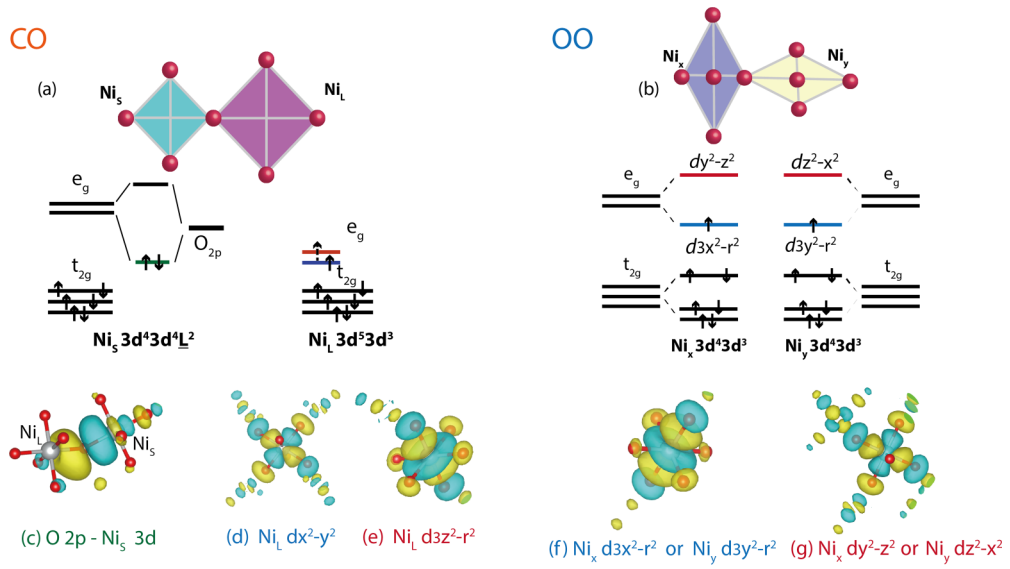

FIG. 5. Schematic electronic level diagrams of Ni ions in HNO: (a) CO between Ni_S and Ni_L in CO. (b) JT distortion on Ni_x and Ni_y in OO. Dotted arrows represent the hopping electrons. Wannier functions: (c) O $2p$-like MLWF with a strong hybridization tail on Ni_S sites. (d) Ni_L $d_{x^2-y^2}$. (e) Ni_L $d_{3z^2-r^2}$. (f) Ni_x $d_{3x^2-r^2}$ or Ni_y $d_{3y^2-r^2}$. (g) Ni_x $d_{y^2-z^2}$ or Ni_y $d_{z^2-x^2}$.

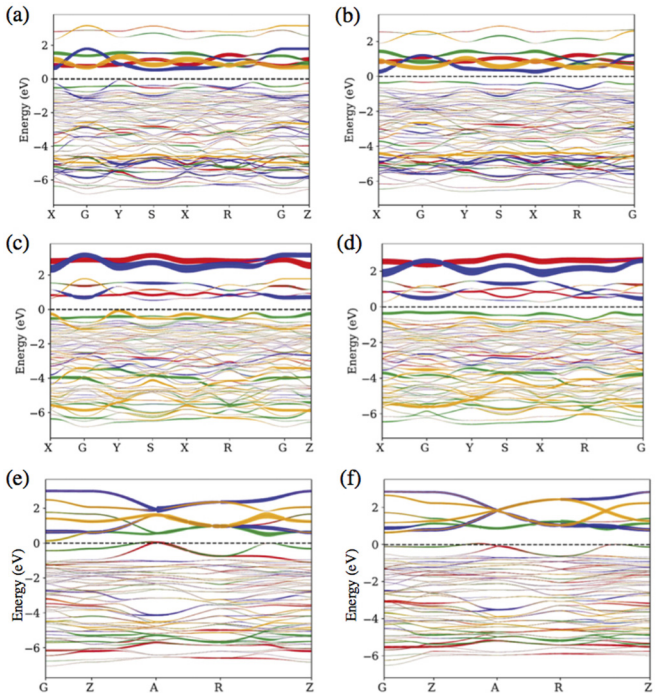

FIG. 6. Band structure (A-AFM) projected on (a) $\epsilon = -2.1\%$ CO Ni_S e_g. (b) $\epsilon = 4.2\%$ CO Ni_S e_g. (c) $\epsilon = -2.1\%$ CO Ni_L e_g. (d) $\epsilon = 4.2\%$ CO Ni_L e_g. (e) $\epsilon = -2.1\%$ OO Ni_x e_g. (f) $\epsilon = 4.2\%$ OO Ni_x e_g. In (a)–(d), green: $d_{3z^2-r^2}$, major spin; yellow: $d_{x^2-y^2}$, major spin; red: $d_{3z^2-r^2}$, minor spin; blue: $d_{x^2-y^2}$, minor spin. In CO Ni_S [(a) and (b)], all these e_g orbitals are mostly above Fermi energy but are mixed with O $2p$ below Fermi energy. In CO Ni_L [(c) and (d)], two major spins e_g (green and yellow) are below Fermi energy, and two minor spins e_g (blue and red) are above Fermi energy. In OO Ni_x [(e) and (f)], $d_{3x^2-r^2}$ (red, major spin) is below Fermi energy, and $d_{3x^2-r^2}$ (blue, minor spin), $d_{y^2-z^2}$ (green, major spin), and $d_{x^2-y^2}$ (yellow, minor spin) are mostly above Fermi energy.

Fig. 5(b)], the $d_{y^2-z^2}$ state has higher energy, and the $d_{3x^2-r^2}$ state has lower energy.

In the OO structure, the Ni_x $d_{3x^2-r^2}$ and $d_{y^2-z^2}$ orbitals in the major-spin channel are below and above the Fermi energy, respectively, and are separated due to a JT splitting, as shown in Figs. 6(e) and 6(f). The e_g states in the minor-spin channel are also mostly unoccupied. Therefore, the gap in the OO phase can be enhanced by the JT distortion. Further increasing tensile strain to the OO phase can enlarge the JT distortion and then increase the band gap, consistent with our calculation results in Fig. 1(b).

IV. CONCLUSION

This paper presented the effects of biaxial strain on CO and OO in HNO epitaxial films. At the point of 4.8% tensile strain, a first-order phase transits between CO and OO. The tensile strain suppresses the breathing mode and enhances the in-plane JT mode. It also enhances the trilinear coupling involving the octahedron rotation modes and the JT mode, which favors the JT mode as tensile strain increases. The JT distortion modulates OO with the e_g electrons occupying the $d_{3x^2-r^2}$ and $d_{3y^2-r^2}$ orbital alternately.

The different types of electronic configurations in these two phases were explored. For the CO phase, the breathing distortion leads to different Ni-O octahedral volumes and e_g/t_{2g} splitting, resulting in a charge transfer between Ni_S and Ni_L. Ni_L has a lower e_g energy level; thus, it has a higher occupation of $3d^8$. The strong hybridization between O $2p$ and Ni_S leads to $3d^8\underline{L}^2$ in Ni_S. For the OO phase, the JT splitting shifts the e_g energy down below the Fermi energy, thus forming a staggered OO. The unoccupied orbitals also form hybridized states with O $2p$, leading to a $3d^8\underline{L}$ electronic configuration. Therefore, this CO to OO phase is accompanied by a $3d^8 + 3d^8\underline{L}^2 \rightarrow 2\times 3d^8\underline{L}$ charge redistribution. As the

tensile strain increases, the band gap first decreases in the CO phase and then increases in the OO phase. Meanwhile, the breathing mode with CO is destroyed, and an in-plane staggered JT mode with OO is developed.

ACKNOWLEDGMENTS

We thank A. Mercy, Ph. Ghosez, and E. Bousquet for their valuable suggestions. This work was supported by the National Key Basic Research Program of China (Grant No. 2014CB921001), the National Key Research and Development Program of China (Grant No. 2017YFA0303604), the National Natural Science Foundation of China (Grants No. 11721404 and No. 11674385), the Key Research Program of Frontier Sciences of the Chinese Academy of Sciences (Grant No. QYZDJ-SSW-SLH020), and the Strategic Priority Research Program (B) of the Chinese Academy of Sciences (Grant No. XDB07030200).

[1] S. Middey, J. Chakhalian, P. Mahadevan, J. Freeland, A. Millis, and D. Sarma, Annu. Rev. Mater. Res. **46**, 305 (2016).
[2] M. L. Medarde, J. Phys.: Condens. Matter **9**, 1679 (1997).
[3] S. Catalano, M. Gibert, V. Bisogni, O. E. Peil, F. He, R. Sutarto, M. Viret, P. Zubko, R. Scherwitzl, A. Georges, G. A. Sawatzky, T. Schmitt, and J.-M. Triscone, APL Mater. **2**, 116110 (2014).
[4] J. A. Alonso, J. L. García-Muñoz, M. T. Fernández-Díaz, M. A. G. Aranda, M. J. Martínez-Lope, and M. T. Casais, Phys. Rev. Lett. **82**, 3871 (1999).
[5] I. I. Mazin, D. I. Khomskii, R. Lengsdorf, J. A. Alonso, W. G. Marshall, R. M. Ibberson, A. Podlesnyak, M. J. Martínez-Lope, and M. M. Abd-Elmeguid, Phys. Rev. Lett. **98**, 176406 (2007).
[6] H. Park, A. J. Millis, and C. A. Marianetti, Phys. Rev. Lett. **109**, 156402 (2012).
[7] S. Johnston, A. Mukherjee, I. Elfimov, M. Berciu, and G. A. Sawatzky, Phys. Rev. Lett. **112**, 106404 (2014).
[8] V. Bisogni, S. Catalano, R. J. Green, M. Gibert, R. Scherwitzl, Y. Huang, V. N. Strocov, P. Zubko, S. Balandeh, J.-M. Triscone *et al.*, Nat. Commun. **7**, 13017 (2016).
[9] H. Chen, D. P. Kumah, A. S. Disa, F. J. Walker, C. H. Ahn, and S. Ismail-Beigi, Phys. Rev. Lett. **110**, 186402 (2013).
[10] J. M. Torriss and M. Chaker, Sci. Rep. **7**, 40915 (2017).
[11] L. Wang, S. Ju, L. You, Y. Qi, Y.-w. Guo, P. Ren, Y. Zhou, and J. Wang, Sci. Rep. **5**, 18707 (2015).
[12] F. Y. Bruno, K. Z. Rushchanskii, S. Valencia, Y. Dumont, C. Carrétéro, E. Jacquet, R. Abrudan, S. Blügel, M. Ležaić, M. Bibes, and A. Barthélémy, Phys. Rev. B **88**, 195108 (2013).
[13] J. M. Rondinelli, S. J. May, and J. W. Freeland, MRS Bull. **37**, 261 (2012).
[14] J. H. Lee, K. T. Delaney, E. Bousquet, N. A. Spaldin, and K. M. Rabe, Phys. Rev. B **88**, 174426 (2013).
[15] A. Mercy, J. Bieder, J. Íñiguez, and P. Ghosez, Nat. Commun. **8**, 1677 (2017).
[16] Z. He and A. J. Millis, Phys. Rev. B **91**, 195138 (2015).
[17] G. Kresse and D. Joubert, Phys. Rev. B **59**, 1758 (1999).
[18] G. Kresse and J. Furthmüller, Phys. Rev. B **54**, 11169 (1996).
[19] S. L. Dudarev, G. A. Botton, S. Y. Savrasov, C. J. Humphreys, and A. P. Sutton, Phys. Rev. B **57**, 1505 (1998).
[20] J. Varignon, M. N. Grisolia, J. Íñiguez, A. Barthélémy, and M. Bibes, npj Quantum Mater. **2**, 21 (2017).
[21] A. Hampel and C. Ederer, Phys. Rev. B **96**, 165130 (2017).
[22] A. A. Mostofi, J. R. Yates, Y.-S. Lee, I. Souza, D. Vanderbilt, and N. Marzari, Comput. Phys. Commun. **178**, 685 (2008).
[23] B. J. Campbell, H. T. Stokes, D. E. Tanner, and D. M. Hatch, J. Appl. Crystallogr. **39**, 607 (2006).
[24] Y. Gu, K. Rabe, E. Bousquet, V. Gopalan, and L.-Q. Chen, Phys. Rev. B **85**, 064117 (2012).
[25] A. T. Zayak, X. Huang, J. B. Neaton, and K. M. Rabe, Phys. Rev. B **74**, 094104 (2006).
[26] J. A. Alonso, M. J. Martínez-Lope, M. T. Casais, M. A. G. Aranda, and M. T. Fernández-Díaz, J. Am. Chem. Soc. **121**, 4754 (1999).
[27] P. V. Balachandran and J. M. Rondinelli, Phys. Rev. B **88**, 054101 (2013).
[28] J. Varignon, N. C. Bristowe, E. Bousquet, and P. Ghosez, Sci. Rep. **5**, 15364 (2015).
[29] H. Raebiger, S. Lany, and A. Zunger, Nature (London) **453**, 763 (2008).